A back-projection autofocus algorithm based on flight trajectory optimization for synthetic aperture radar imaging

Jamal Saeedi · Karim Faez

Abstract In this paper, a new autofocus algorithm is presented for back-projection (BP) image formation of synthetic aperture radar (SAR) imaging. The approach is based on maximizing a cost function obtained by prominent points in different sub-apertures of constructed SAR image by varying the flight trajectory parameters. While image-quality-based autofocus approach together with BP algorithm can be computationally intensive, we use approximations that allow optimal corrections to be derived. The approach is applicable for focusing different signal processing algorithms by obtaining modified flight trajectory parameters. Different examples demonstrate the effectiveness of the new autofocus approach applied to the frequency modulated continuous wave mode SAR dataset.

Keywords Synthetic aperture radar · Autofocus algorithm · Back-projection · Frequency modulated continuous wave · Strip-map

1 Introduction

Synthetic aperture radar (SAR) is an imaging technique, which uses the relative motion between a radar antenna and target area, to obtain better spatial resolution as compared to traditional beam scanning methods. SAR can produce high-resolution imagery of a wide area using a small antenna and a large bandwidth. The motion of the radar platform synthesizes a very large aperture using the data recorded from the radar echoes of a series of radar transmissions. This large synthetic aperture provides fine resolution in the flight direction or azimuth, although a fine resolution in range is provided by a large bandwidth. Reconnaissance, surveillance, navigation and guidance, treaty verification and nonproliferation, interferometry,

J. Saeedi · K. Faez (✉)
Electrical Engineering Department, Amirkabir University of Technology (Tehran Polytechnic),
424, Hafez Ave., Tehran, Iran
e-mail: kfaez@aut.ac.ir

J. Saeedi
e-mail: jamal.saeedi@yahoo.com

 ⓐ Springer

foliage and ground penetration (Krishnan 2000; Gilmore 2004), moving target indication, change detection, and environmental monitoring are some examples of SAR applications (Sandia 2006). Capability of forming images in day or night under all weather conditions is the most salient feature of SAR.

The SAR processing algorithms assume that the radar platform moves at a constant speed in a straight trajectory. Nevertheless, this is not true as the platform experiences a variety of deviations from the ideal path in actual data collection. These deviations introduce errors in the stored data, which decrease SAR image quality. Coherent processing of SAR data requires precise knowledge of the relative geometric between the flight trajectory and the scene being imaged. This geometry information is typically acquired using navigation systems such as inertial measurement units (IMUs) and global positioning system (GPS) receivers. In a typical SAR system, navigation data are employed for motion compensation (MC). To achieve highly precise MC, motion measurements have to be achieved at sub-wavelength scale from pulse to pulse. However, these sensors could be too expensive and may not provide the accuracy required for high-resolution imaging. Thus, navigation measurements usually provide only coarse MC. Consequently, signal based MC, i.e., autofocus, is a crucial step that provides a necessary enhancement to IMU/GPS devices, especially for airborne SAR processing, to achieve a very fine resolution. The automatic estimation and compensation of phase errors in SAR image formation using the information in raw data is referred as autofocus algorithm.

Autofocus methods typically can be divided into two categories including the parametric and non-parametric methods. Parametric autofocus methods estimate a set of coefficients that parameterize a model, which is used to compensate for phase errors. Non-parametric methods estimate a phase function, which is used to compensate for phase errors. Many kinds of autofocus algorithms have been proposed over the years. Map-drift (Wahl et al. 1994), phase-gradient (Oliver and Quegan 1999), and prominent point processing (Wahl et al. 1994) are some of the more common autofocus methods. Conventional autofocus methods are applicable for the frequency domain data processing algorithms such as range-Doppler algorithm (RDA), and frequency scaling algorithm (FSA), and cannot be applied by back-projection (BP) image formation method. In the frequency domain algorithms, a coarse MC using navigation data is performed followed by an autofocus algorithm for estimating remaining phase error. However, BP algorithm uses the navigation data directly in the image formation procedure, and therefore conventional autofocus algorithm cannot be used.

The BP image formation algorithm places few limitations on SAR imaging; therefore, it is desirable to have an autofocus algorithm that is likewise unconstrained. This paper presents an autofocus method that is accordant with BP. In the literature, some works reported the usage of autofocus for BP algorithm (Hellsten et al. 2010; Liu et al. 2011; Ash 2012). Hellsten et al. (2010) proposed a method in which antenna path parameters is determined in order to get focused image using fast factorized BP algorithm. Antenna path parameters are determined in different sub-apertures using an optimization-based method in which the cost function is the integral of sub-image energy. Liu et al. (2011) suggest a metric-based autofocus for BP algorithm in which only the platform speed is varied in order to get focused image. The platform speed is optimized by minimizing the entropy of SAR image, which is constructed by BP algorithm. Ash (2012) proposes an autofocus routine for BP imaging for spotlight-mode SAR data. In this method, optimal phase error correction for each pulse is determined in a closed form within the coordinate descent framework, where focusing the image is equivalent to maximize the sharpness in standard BP algorithm.

The problem with the previous autofocus methods for BP algorithm is that the computational load of the metric-based method incorporating with the BP algorithm is generally high. This is because in each iteration of the optimization algorithm there should be an image

or sub-image constructed by BP algorithm, which has high computational complexity. In addition, they have specific assumptions about the imaging geometry such as spotlight or circular modes. To improve the efficiency but to keep the advantages, we present a new metric-based approach to modify the flight trajectory for BP imaging. This new method makes no assumption about the imaging geometry. Knowing the initial path of the SAR sensor using the navigation data, we can obtain the optimum trajectory by optimizing a proper objective function. The flight trajectory is modeled using polynomial functions in a three dimensional space. Specifically, we propose an approximate model to obtain the cost function for optimization without using BP algorithm in order to lower the computational complexity.

Constructions of very small SAR systems are possible by using a linear frequency modulated continuous wave (LFM-CW) signal in the radar transmitter (Meta et al. 2004; Edrich 2004; Meta et al. 2006; Zaugg et al. 2006; Partida et al. 2008; Edwards et al. 2008). Combined with an analog dechirp in the receiver, these systems can be made with hardware which is simpler, cheaper, and consumes less power than the conventional pulsed SAR systems. This enables the use of low cost SARs on small-unmanned aircraft systems (UAS), which makes possible SAR imagery to be obtained in harsh climates or in environments too dangerous for manned aircraft or expensive SAR systems. The motion error problem is particularly apparent to the UAS SAR, because it is easily disturbed by the atmospheric turbulence due to its small size and lightweight. Moreover, the UAS SAR may not be equipped with a highly accurate navigation system due to weight capacity restriction (Wang et al. 2009). Therefore, for the UAS SAR imaging, MC strategies are important and advisable based on the raw data or autofocus. For this reason, we have considered SAR in LFM-CW mode for theoretical discussions; however, it can be generalized for pulsed mode SAR. Real data from two different SAR systems in LFM-CW mode are also used for experimental results.

The remainder of this paper is organized as follows. The fundamental of SAR signal processing in LFM-CW mode is briefly reviewed in Sect. 2. Section 3 gives the description of the MC using navigation data. In Sect. 4, trajectory optimization for BP image formation is presented. Section 5 illustrates experimental results. Finally, conclusions are given in Sect. 6.

2 LFM-CW synthetic aperture radar signal processing

In this section, first we will describe how to model the transmitted and received signal based on LFM-CW. Then, back projection algorithm for image formation of received SAR signal is explained. SAR system illuminates the scene with a series of coherent pulses while passing by a target. The series of radar echoes from the target area are digitized and processed to form the image. Before the SAR signal is generated, a number of important system parameters should be determined, including carrier frequency, bandwidth, pulse length, and pulse repetition frequency (PRF). The transmitted signal is a LFM waveform, where the signal spans the bandwidth over the pulse length. This cycle is repeated at the PRF. The SAR signal is usually generated at or near baseband and then mixed up to the desired operating frequency before transmission. The LFM transmit signal can be expressed as:

$$s_t(t) = A(t) \exp(j(2\pi f_0 t + \pi k_r t^2 + \varphi_0)) \tag{1}$$

where $A(t)$ is the signal amplitude as a function of time t and defines the pulse length with a rect function, k_r is the chirp rate, f_0 is the frequency at the beginning of the chirp, and φ_0 is the starting phase which can usually be neglected.

In the transmission chain, a power amplifier increases the power to a specified level. The transmitted signal needs to have enough power so that the signal-to-noise-ratio (SNR) is large enough to generate a good image. The amplified signal transmitted through the antenna propagates to the target area. A very small portion of the transmit signal is reflected back to the radar. By neglecting the time-scaling influences on the pulse envelope, the echoed signal from target can be expressed as:

$$s_r(t, \eta) = A'(t) \exp(j(2\pi f_0(t - \tau) + \pi k_r(t - \tau)^2 + \varphi_0)) \tag{2}$$

where t is fast time, η is slow time (or azimuth time), and $A'(t)$ is an attenuated version of $A(t)$ and τ is the two-way time of flight to the target at range R. It should be mentioned that τ is a function of t and η and is obtained using the following:

$$\tau(t, \eta) = \frac{2R(t, \eta)}{c} = \frac{2\sqrt{r_0^2 + (v(t + \eta) - x_0)^2}}{c} \tag{3}$$

where v is the platform velocity, r_0 is the range of closest approach, x_0 is target position in azimuth direction, and c is the light speed.

In the pulsed mode, the pulse duration is short about a few microseconds; however, for the LFM-CW mode, the pulse duration is about milliseconds, corresponding to the pulse repetition interval. Therefore, the number of samples for LFM-CW mode could be too many. The dechirp-on-receive technology is generally used in the LFM-CW SAR system to reduce the sampling requirements and data rate (Meta et al. 2007; Carrara et al. 1995).

With an analog dechirp, the received signal is mixed with a copy of the transmit signal, and low-pass filtered in hardware, which is mathematically equivalent to multiplying (1) by the complex conjugate of (2). This results in the dechirped signal:

$$s_{dc}(t, \eta) = s_t.s_r^* = A''(t) \exp(j(2\pi f_0\tau + 2\pi k_r t.\tau - \pi k_r \tau^2)) \tag{4}$$

SAR systems digitize this data and either store it on board, transmit it to a ground station, or process it on-board. For range compression of de-chirped LFM signal, only one FT is necessary (Franceschetti and Lanari 1999). Assuming no motion during the chirp is equivalent to assuming that R is not a function of t. Thus, the range-compressed signal is obtained using the following:

$$s_{rc}(f_r, \eta) = \int_\tau^{\tau+T} s_{dc}(t, \eta). \exp(-j2\pi f_r t)dt = T.\text{sinc}(T(f_r - k_r\tau))$$
$$. \exp(j\pi(k_r\tau.T - f_r T + k_r\tau^2 + 2f_0\tau - 2f_r\tau)) \tag{5}$$

where T is pulse width, and f_r is the frequency in range direction.

Since the peak value of the range-compressed signal lies on $f_r = k_r.\tau$, (5) can be simplified as follows:

$$s_{rc}(f_r, \eta) \approx T.\text{sinc}(T(f_r - k_r\tau)). \exp(j\pi(2f_0\tau - f_r\tau)) \tag{6}$$

2.1 Back-projection algorithm

In this subsection, we focus on time-domain reconstruction algorithms for LFM-CW SAR. The main advantage of these algorithms when compared with frequency-domain algorithms is their natural use of the available information on the sensor's trajectory, which makes them best suited when facing highly nonlinear trajectories of the platform (Frey et al. 2009).

Time-domain correlation (TDC) algorithm uses the raw data directly, without range-compression. The platform position for each sample of raw data is used. In this case, SAR

image from a point target is formed using the following formula:

$$im(x_0, y_0, z_0) = \sum_t \sum_\eta s_{dc}(t, \eta) \exp(j.\Phi_{x_0,y_0,z_0}(t, \eta)) \tag{7}$$

where $s_{dc}(t, \eta)$ is the dechirped signal expressed in (4), $(x_0, y_0, z_0)$is the coordinate of a point target on the ground (usually there is no information about the elevation of a target on the ground, and z_0 can be approximated with zero), and $\Phi(t, \eta)$ is the conjugate of the signal phase in (4), which can be expressed as:

$$\Phi_{x_0,y_0,z_0}(t, \eta) = -(2\pi f_0 \tau_{x_0,y_0,z_0}(t, \eta) + 2\pi k_r t.\tau_{x_0,y_0,z_0}(t, \eta) - \pi k_r \tau_{x_0,y_0,z_0}^2(t, \eta)) \tag{8}$$

where $\tau_{x_0,y_0,z_0}(t, \eta)$ is the two-way time of flight to the target at position (x_0, y_0, z_0) on the ground, and it is obtained using the following:

$$\tau_{x_0,y_0,z_0}(t, \eta) = \frac{2R_{x_0,y_0,z_0}(t, \eta)}{c} = \frac{2\sqrt{(H - z_0)^2 + y_0^2 + (v(t + \eta) - x_0)^2}}{c} \tag{9}$$

where v is the platform velocity, H is the flight altitude and c is the light speed. It should be mentioned that for the rest of the paper, we have supposed τ_{x_0,y_0,z_0} as τ_0 for simplicity.

This is a very exact method, but it is very computationally taxing, which is rarely used in practice. BP normally operates on the range-compressed data. For dechirped SAR, interpolation and range compression can be performed by means of zero-padding and a range FT. Using the start and stop approximation, τ_0 does not depend in fast time t, and we can rewrite (7) as:

$$im(x_0, y_0, z_0) = \sum_\eta \exp(-j2\pi f_0 \tau_0) \exp(j\pi k_r \tau_0^2) \sum_t s_{dc}(t, \eta) \exp(-j2\pi k_r \tau_0 t) \tag{10}$$

Using the definition of discrete FT, we can obtain the following formula:

$$im(x_0, y_0, z_0) = \sum_\eta s_{rc}(k_r \tau_0, \eta).\exp(-j2\pi f_0 \tau_0) \exp(j\pi k_r \tau_0^2) \tag{11}$$

where s_{rc} is the range-compressed SAR data using range FT, interpolated to $k_r.\tau_0$.

3 Motion compensation using navigation data

The SAR processing method described in Sect. 2 assume that the platform moves at a constant speed in a straight line. Translational motion causes a platform displacement from the nominal, ideal path as shown in Fig. 1a. This results in the target scene changing in range during data collection. This range shift also causes inconsistencies in the target phase history. A target located at range R_0, measured at range $R = R_0 + \Delta R_0$ results in a phase error in dechirped signal (4) as:

$$s_{\Delta dc}(t, \eta) = A''(t) \exp(j(2\pi f_0(\tau_0 + \Delta\tau_0) + 2\pi k_r t.(\tau_0 + \Delta\tau_0) - \pi k_r(\tau_0 + \Delta\tau_0)^2)) \tag{12}$$

where $\tau_0 = 2R_0/c$, and $\Delta\tau_0 = 2\Delta R_0/c$.

3.1 Flight trajectory estimation using GPS data

The motion errors can be compensated if the platform motion is measured using an onboard INS/GPS sensor. In general, the motion data is collected at a much slower rate than
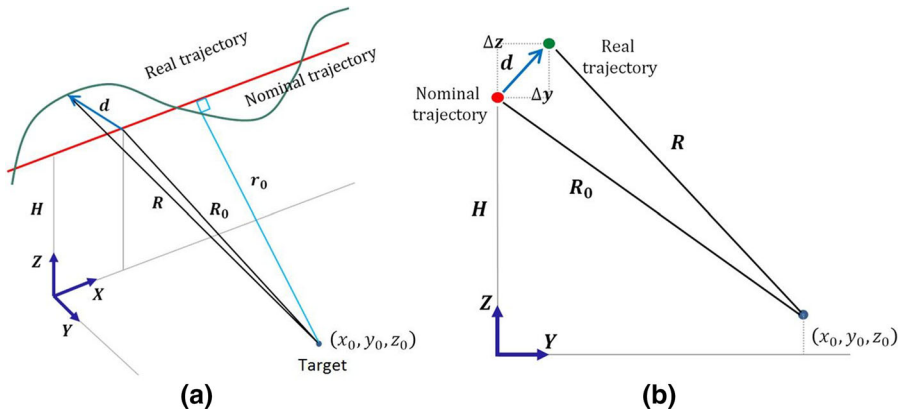
Fig. 1 **a** Stripmap SAR geometry, **b** normal plane of the ideal trajectory

the SAR data. The motion data must be interpolated so that every sample of SAR data has corresponding position information. Each data point also needs to have a corresponding location on the ideal path to find the error for compensation. Using the GPS to Cartesian transform, we can find the real trajectory of SAR platform. Figure 2 shows a sample of 10 Hz GPS data and corresponding flight trajectory in three-dimensional space. The flight trajectory obtained by GPS to Cartesian transform has two evident problems: 1) fluctuations of flight trajectory because of GPS error, and 2) altitude bias, because the height information is relative to sea level. These two problems should be resolved for MC. A common and completely reasonable response in selecting an interpolation strategy for improving motion data is to use the following:

$$C(t) = A_0 + A_1 t + A_2 t^2 + A_3 t^3 + \cdots + A_N t^N \tag{13}$$

a simple polynomial as the analytic function approximating the data in the interpolator (Horemuz and Andersson 2006; Schenewerk 2003). Here, C represents the X, Y, or Z coordinate value, t is time and A_0 through A_N are the coefficients of the polynomial, which are adjusted to fit the measured motion data.

The values of the coefficients will be determined by fitting the polynomial to the source data. This can be done by minimizing an error function that measures the misfit between the $C(t)$ (for any given value of A) and the source data points. One simple choice of error function, which is widely used, is given by the sum of the squares of the errors. There remains the problem of choosing the order N of the polynomial, which affects the result of phase error compensation. Here, we have used a metric-based approach to automatically determine the polynomial order, which will be described in next section.

In addition to polynomial fitting, we have used nadir return to improve the height estimation and remove GPS altitude bias. Note that SAR platform travels forward in the flight direction with the nadir directly beneath the platform. The platform height can be accurately estimated from the range-compressed SAR data. To illustrate, Fig. 3 plots a sample of range-compressed data. The nadir echo is evident in the range-compressed data where it corresponds to the top of the horizontal dark band in the plot. Note that there is no return signal for slant ranges shorter than the platform height.

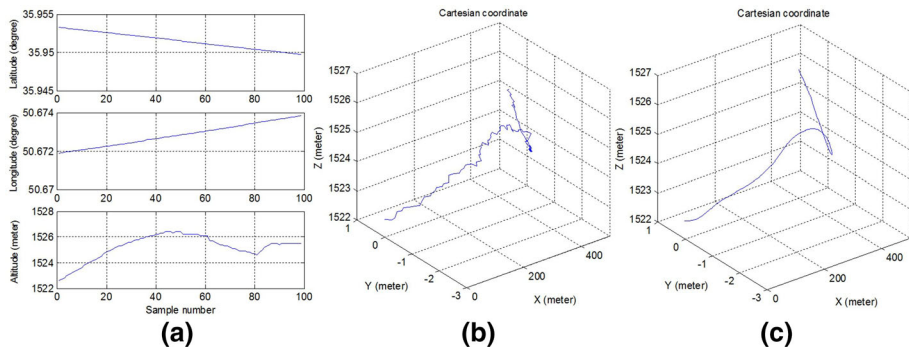In the following, the theoretical treatment of full MC using navigation data for RDA is described.

Fig. 2 **a** A sample of 10 Hz GPS data for 10 s flight, **b** corresponding flight trajectory, and **c** flight trajectory after fitting 10-order polynomial functions
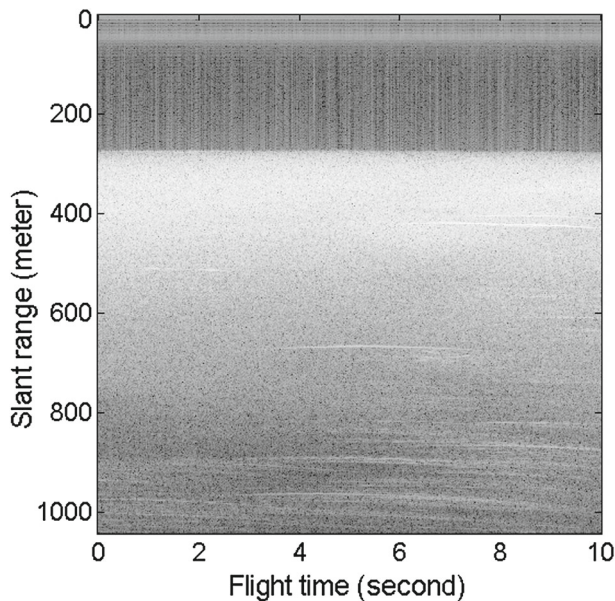

Fig. 3 Range-compressed data with nadir return at top of the image (slant range extends from the *top* of the image)

3.2 Full motion compensation using flight trajectory information

For time-domain reconstruction algorithms including TDC and BP, we can directly use the motion data to compensate the phase error. Here, the strip-map SAR geometry of Fig. 1a is assumed. The instantaneous motion error vector d, defined by the displacement between the real and nominal trajectories, is $[\Delta x(\eta), \Delta y(\eta), \Delta z(\eta)]$, where $\Delta y(\eta)$ and $\Delta z(\eta)$ represent the cross-track displacement as shown in Fig. 1b. Knowing the coordinates of target (x_0, y_0, z_0), the real trajectory, and the nominal trajectory, the distances R and R_0 can be calculated from geometry:

$$R(\eta; x_0, y_0, z_0) = \sqrt{(v.\eta + \Delta x(\eta) - x_0)^2 + (\Delta y(\eta) - y_0)^2 + (H + \Delta z(\eta) - z_0)^2}$$

$$= R_0(\eta; x_0, y_0, z_0) + \Delta R_0(\eta; x_0, y_0, z_0) \tag{14}$$

$$R_0(\eta; x_0, y_0, z_0) = \sqrt{(v.\eta - x_0)^2 + y_0^2 + (H - z_0)^2} \tag{15}$$

However, for frequency domain algorithms it is not possible to directly use the motion data for phase error correction. The traditional MC method for RDA involves two steps. First, the corrections are calculated for a reference range, R_{ref}, usually in the center of the swath. The first step of phase correction is as:

$$H_{mc_1} = \exp(-j2\pi f_0 \Delta \tau_{ref}) \tag{16}$$

where $\Delta \tau_{ref} = 2\Delta R_{ref}/c$. Then, the SAR data is range-compressed. This is the center-beam approximation (Cumming et al. 2003) and is used in many MC algorithms. A second order correction is applied to each range, according to the differential correction from the reference range. For each R, ΔR is calculated and the correction is formed as:

$$H_{mc_2} = \exp(-j2\pi f_0 (\Delta \tau_0 - \Delta \tau_{ref})) \tag{17}$$

This method introduces error after the range compression, which is not acceptable for a high-resolution SAR system. In this study, an efficient MC method is proposed to apply on the range-compressed data. The range-compressed signal of (12) can be obtained using FT as follows:

$$s_{\Delta rc}(f_r, \eta) \approx T.\mathrm{sinc}(T(f_r - k_r(\tau_0 + \Delta\tau_0))).\exp(j\pi(2 f_0(\tau_0 + \Delta\tau_0) - f_r(\tau_0 + \Delta\tau_0))) \tag{18}$$

Since the peak value of the range compressed signal lies on $f_r = k_r.(\tau_0 + \Delta\tau_0)$, (18) can be simplified as follows:

$$s_{\Delta rc}(f_r, \eta) \approx T.\mathrm{sinc}(T(f_r - k_r(\tau_0 + \Delta\tau_0))).\exp(j\pi(2 f_0(\tau_0 + \Delta\tau_0) - k_r(\tau_0 + \Delta\tau_0)^2)) \tag{19}$$

From (19) we can find a correction filter, which works on the range-compressed data as:

$$H_{mc}(f_r, \eta) = \exp(j\pi(-2 f_0 \Delta\tau_0 + k_r \Delta\tau_0^2 + 2k_r \tau_0 \Delta\tau_0)) \tag{20}$$

After the filtering, the range-compressed data becomes:

$$s_{\Delta rc}(f_r, \eta) \approx T.\mathrm{sinc}(T(f_r - k_r(\tau_0 + \Delta\tau_0))).\exp(j\pi(2 f_0 \tau_0 - k_r \tau_0^2)) \tag{21}$$

For exactly focusing the data, an azimuth dependent interpolation should be used to compensate the range shift due to motion error. This is similar to the Stolt interpolation applied in omega-k algorithm (Cumming and Wong 2005). The interpolation is defined as:
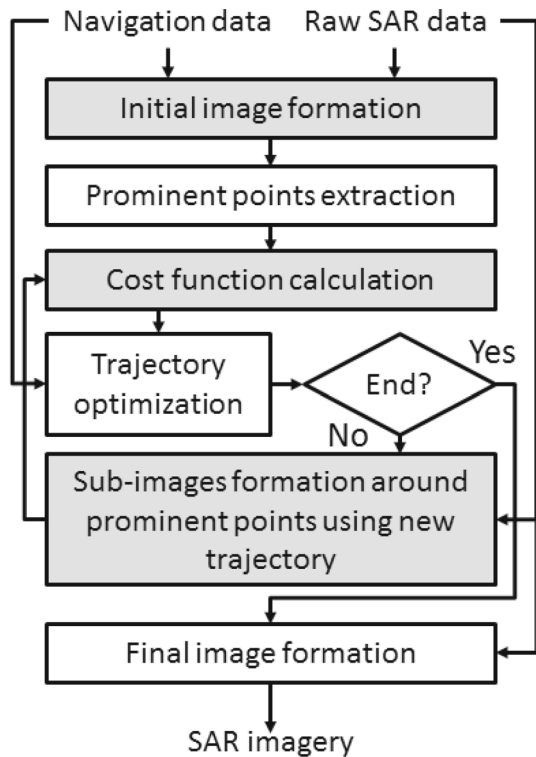
$$f_r - k_r(\tau_0 + \Delta\tau_0) \rightarrow f_r' - k_r \tau_0 \tag{22}$$

To achieve perfect range compression and registration, the mapping in (22) transforms the original range frequency variable f_r into the new range frequency variable, f_r'. By doing this, (21) can be expressed as:

$$s_{rc}(\tau, \eta) \approx T.\mathrm{sinc}(T(f_r - k_r \tau_0)).\exp(j\pi(2 f_0 \tau_0 - k_r \tau_0^2)) \tag{23}$$

At the end, we have a range-compressed signal with compensated phase error.

4 Trajectory optimization for back-projection image formation

In this section, the proposed autofocus method for BP image formation is presented. We first derive the general autofocus model for the BP algorithm. Then, the general model is approximated using the RDA to improve the computational complexity.

4.1 General autofocus model

The proposed autofocus model is based on trajectory optimization using prominent points (PPs) in different sub-apertures of constructed SAR image. This new method makes no assumption about the imaging geometry. Knowing the initial path of the SAR sensor using the navigation data, we can obtain the optimum trajectory by optimizing a proper objective function. Specifically, the proposed autofocus method involves analysis of the formed image (i.e., range and azimuth compressed) in order to estimate proper correction factors to modify flight trajectory. Figure 4 gives block diagram of the proposed autofocus for BP algorithm. The flight trajectory optimization is composed of the following essential steps:

4.1.1 Initial image formation

In first step, an initial SAR image is formed using BP algorithm. BP algorithm formulated in (20) uses complex raw SAR data and initial flight trajectory. Initial flight trajectory is obtained from the navigation data by GPS to Cartesian transform after two modifications, which are described in Sect. 3.

4.1.2 Prominent points extraction

In this step, the initial SAR image is divided by N sub-apertures and in each sub-aperture, one PP is selected. First, the initial SAR image is smoothed by a Gaussian filter and de-speckled by median filtering. Then, local maximums are obtained in each sub-aperture. Finally, a point with maximum average peak-side-lobe level-ratio (PSLR) in both azimuth and range directions is selected as a PP in each sub-aperture.

The PPs are used to obtain the cost function in the trajectory optimization process. The cost function should be a function of different parts of flight trajectory. For this reason, we have considered different sub-apertures for selecting PPs. PPs selection can also be extended to different range blocks for improving the cost function calculation. Specifically, we can divide SAR image into N sub-apertures and M range blocks. In this way, we can use more than one PP in each sub-aperture for cost function calculation.

4.1.3 Cost function calculation

After finding the PPs in the SAR image, a cost function is obtained for flight trajectory optimization. Phase error collected in SAR raw data due to non-linear flight trajectory, in one-hand results in widening the target response in azimuth direction, and in another hand results in lowering the target peak level. Therefore, a proper cost function should consider these effects.

It can be shown theoretically that a SAR image has its maximum amplitude without any phase error. The magnitude of a point target of a SAR image with phase error using BP algorithm can be written as follows:

$$
im(x_0, y_0, z_0) = \sum_{\eta} |s_{\Delta rc}(k_r \tau_0, \eta). \exp(-j2\pi f_0 \tau_0) \exp(j\pi k_r \tau_0^2)| = \sum_{\eta} |s_{\Delta rc}(k_r \tau_0, \eta)|
$$

$$
\sum_{\eta} |\sigma_0.T.\mathrm{sinc}(T(k_r \tau_0 - k_r(\tau_0 + \Delta \tau_0))). \exp(j\pi(2f_0(\tau_0 + \Delta \tau_0) - k_r \tau_0(\tau_0 + \Delta \tau_0)))|
$$

$$
= \sum_{\eta} |\sigma_0.T.\mathrm{sinc}(T(k_r \tau_0 - k_r(\tau_0 + \Delta \tau_0)))| = \sum_{\eta} |\sigma_0.T.\mathrm{sinc}(T(-\boldsymbol{k_r \Delta \tau_0}))|
$$

$$
\tag{24}
$$

where σ_0 is the radar cross section of point target at coordinate x_0, y_0, z_0, T is pulse width, τ_0 is delay to target, k_r is chirp rate, and $\Delta \tau_0$ is phase error.

Since the Sinc function has its maximum value at zero, the resulting magnitude of (24) is decreased because of the phase error $\Delta \tau_0$. It can be concluded that the target peak level is proportional with phase error and should be included in cost function calculation. It is well known that the phase error causes target defocus in azimuth direction as it can be seen in Fig. 5 (Hellsten et al. 2010; Liu et al. 2011). The target defocus can be measured by integrated sidelobe level ratio (ISLR), which is the ratio between the energy of the mainlobe and that integrated over several (usually 10–20 dB) sidelobes on both sides of the main one. The proposed cost function is defined in order to consider both target peak and target defocus as follows:

$$
Cost = \frac{1}{N} \sum_{i=1}^{N} PP_i \times \mathrm{ISLR}(PP_i)
\tag{25}
$$

where PP_i is the absolute values of PPs in SAR image, ISLR is calculated with center of PPs in azimuth direction, and N is the number of PPs.
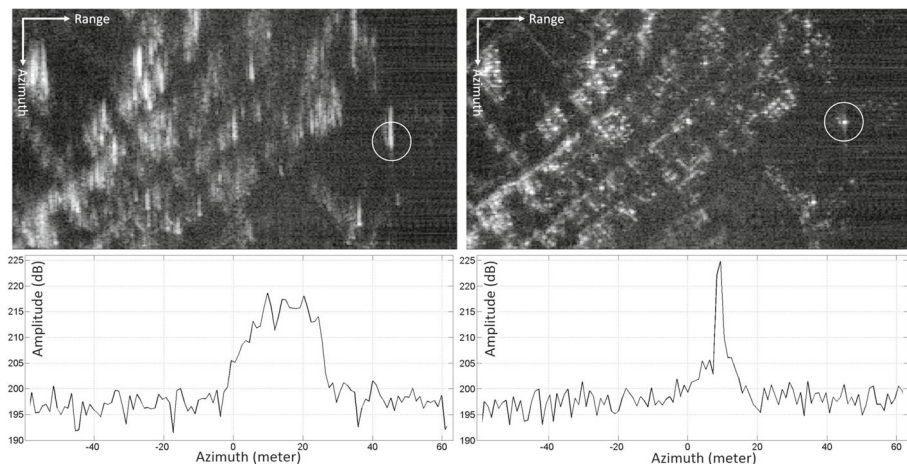
Fig. 5 *Top row*: (*left*) degraded, and (*right*) focused SAR image, *bottom row*, azimuth profiles of point targets highlighted in *white circles*

It should be mentioned that the locations of PPs are updated in each iteration of optimization algorithm. It is simply performed by selecting the maximum values in a neighborhood around previous PPs locations.

4.1.4 Trajectory optimization

In this step, flight trajectory is optimized using the maximization of the cost function defined by (24). To aim this, we have modeled the flight trajectory by polynomial functions:

$$X(t) = X_0(t) + \sum_{i=1}^{N_x} P_x(i).t^i, \, Y(t) = Y_0(t) + \sum_{i=1}^{N_y} P_y(i).t^i, \, Z(t) = Z_0(t)$$
$$+ \sum_{i=1}^{N_z} P_z(i).t^i \qquad (26)$$

where t is the flight time $0 < t < t_f$, P_x, P_y and P_z are polynomial parameters, and X_0, Y_0 and Z_0 are initial flight trajectory obtained by navigation data.

Using the model expressed in (26), we have $P_x + P_y + P_z$ parameters to be optimized. Here, we have used the genetic algorithm (GA) for the optimization problem (Goldberg 1989). This maximization is supposed to be accomplished while satisfying the following constraints:

$$|X(t_f) - X_0(t_f)| \le Th_x, \, |Y(t_f) - Y_0(t_f)| \le Th_y, \, |Z(t_f) - Z_0(t_f)| \le Th_z \qquad (27)$$
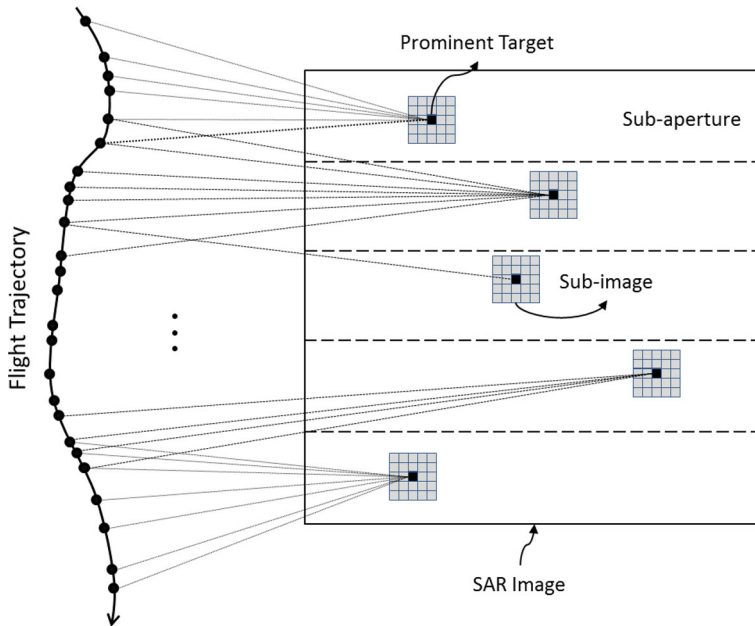
where Th_x, Th_y and Th_z are some thresholds.

Fig. 6 Graphical representation of forming the sub-images in different sub-apertures using BP algorithm

The constraints are considered in the optimization for avoiding large changes in the trajectory.

4.1.5 Sub-images formation

After the first iteration of optimization, there is no need to form the whole SAR image for cost function calculation. Only the sub-images around the PPs are constructed using the BP algorithm (20). Figure 6 gives the graphical representation of forming the sub-images in different sub-apertures using BP algorithm. After forming the sub-images, maximum absolute values around previous locations of PPs are considered as new PPs, and cost function is obtained by (25).

4.1.6 Final image formation

After a predefined iteration, final SAR image is formed using the optimized flight trajectory and BP algorithm.

4.2 Approximate model

The general autofocus model for BP algorithm is derived in the first part. However, this model is not efficient in term of computational complexity. In this part, we focus on the approximations of the general autofocus model, which is mainly based on RDA instead of BP algorithm. We have presented the flowchart of the proposed model in Fig. 7. For the clarity of the proposed algorithm for flight trajectory optimization, we have employed a feasible procedure as follows:
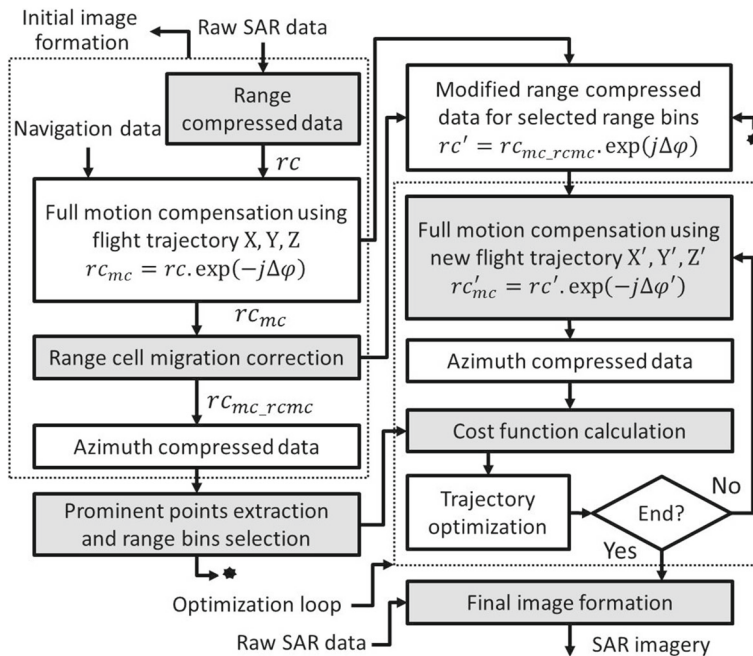
Fig. 7 Flowchart of the proposed autofocus model

4.2.1 Initial image formation

In this step, RDA together with MC are used to generate an initial SAR image for autofocus algorithm. In contrast with the general model, we have used BP algorithm to do the same. The details about the RDA and MC are described in Sects. 2 and 3, respectively.

4.2.2 Prominent points extraction and range bins selection

Similar to the general model, a number of PPs are selected in SAR image for cost function calculation in the optimization loop.

4.2.3 Modified range compressed data

In this step, we have used an inverse procedure after range-cell-migration-correction step in RDA to obtain a modified range-compressed data. By doing this; we can approximately cancel RCM effect in the range-compressed data. In addition, we have only considered range bins around each PP to calculate modified range-compressed data. These two mentioned modifications, decrease computational complexity of generating SAR image in the optimization loop.

4.2.4 Optimization loop

In the optimization loop, we need to generate a SAR image to compute the cost function in order to optimize the flight trajectory. By knowing the position of the PPs in the initial
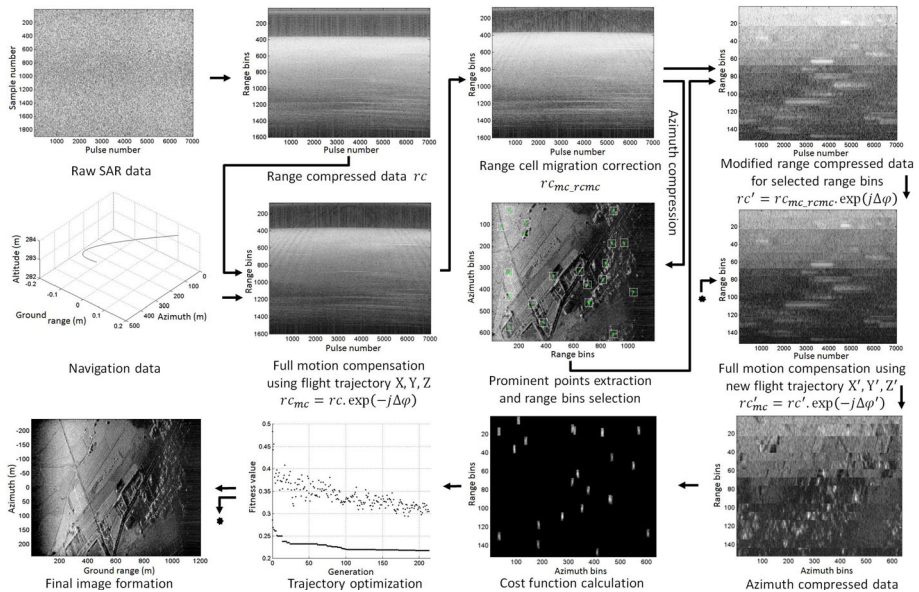
Fig. 8 Graphical representation of the proposed autofocus algorithm

SAR image, we can calculate the cost function in the new SAR image, which is obtained by updated flight trajectory. Cost function calculation and trajectory optimization are similar to the general model case.

4.2.5 Final image formation

After a predefined iteration, the final SAR image is formed using the optimized flight trajectory and BP algorithm.

For better understanding, step-by-step implementation of the proposed autofocus algorithm for a sample LFM-CW SAR data is demonstrated in Fig. 8. Clearly, when compared with the general autofocus model, the computational load of the approximate method is much lower. This autofocus method is advantageous because it requires no general assumptions of platform motion in order to operate. Other methods of autofocus typically only operate on spotlight mode data. In addition, this new method can be used for both time and frequency domain algorithms by providing optimized flight trajectory.

As we have mentioned in previous section, the order N of polynomial in (13) should be selected to obtain initial motion data. Here, we have used the same procedure for flight trajectory optimization in order to determine the order of polynomial for initial trajectory. Specifically, we first run the algorithm for determining the initial trajectory in (26), and then apply the phase error model for trajectory optimization.

4.3 Genetic optimization

Having the flight trajectory model, cost function, and constraints, we need an optimization algorithm to optimize the trajectory. Over the years, many real-parameter optimization algorithms have been developed by using point-by-point (Kirkpatrick et al. 1983; Rao 1984) as well as multi-point approaches (Goldberg 1989; Kennedy and Eberhart 1997). While a point-

by-point approach begins with one guessed solution and updates the solution iteratively for reaching near the optimum solution, a multi-point method deals with a number of solutions in each iteration. Starting with a number of guessed solutions, the multi-point algorithm updates one or more solutions in a synergistic way for steering the population toward the optimum.

In this paper, we have considered GA for the optimization problem. GA is inspired by the nature, and has proved itself to be effective solution to optimization problems. Appropriate setting of control parameters of GA is a key point for its success. In general, some forms of trial-and-error tuning are necessary for each particular instance of optimization problem. In this sub-section, we briefly describe GA.

In GA (Goldberg 1989), a candidate solution for a specific problem is called an individual or a chromosome and consists of a linear list of genes. Each individual stands for a point in the search space, and therefore a possible solution to the problem. A population consists of a finite number of individuals. Each individual is decided by an evaluating system to obtain its fitness value. Based on this fitness value and undergoing genetic operators, a new population is iteratively generated with each successive population referred to as a generation. Three basic genetic operators are sequentially applied to each individual with certain probabilities during each generation, i.e., selection, crossover (recombination), and mutation. First, a number of best individuals are picked based on a user defined fitness function. The remaining individuals are discarded. Next, a number of individuals are selected and paired with each other. Each individual pair generates one offspring by partially exchanging their genes around one or more randomly selected crossing points. At the end, a certain number of individuals are selected and the mutation operations are applied (i.e., a randomly selected gene of an individual abruptly changes its value). The GA is called a population-based technique because instead of operating on a single potential solution, it uses a population of potential solutions.

The larger the population, the greater the diversity of the members of the population, and the larger the area searched by the population. Here, we have used Matlab optimization toolbox for implementation of GA. Based on the experimental results (see Fig. 8) the population size is set to 60 and the generation size is set to 150 for genetic optimization as a good compromise between accuracy and complexity.

5 Experimental results

In this section, we demonstrate results on real data from two different SAR systems. In the first experiment, the raw SAR data with an imaging resolution of 1.5×1 m (range $\times$ azimuth) are collected by an experimental SAR, which was developed by the PARDIS electronic development company in Iran as shown in Fig. 9. A helicopter carried the SAR system. The experimental SAR system operated in C-band (5.20 GHz) with bandwidth 100 MHz. The helicopter flew at a height of about 200–1,000 m, at a speed of 30–60 m/s. At C-band, two identical custom microstrip antennas, each consisting of a 2×8 patch array, are used in a bi-static configuration. The antennas are constructed from two printed circuit boards sandwiched together, a symmetric feed structure on the back of one board and a microstrip patch array on the front of another, with pins feeding the signal through the boards. The antennas are approximately 4"$\times$12" and have an azimuth 3 dB beamwidth of $11°$ and an elevation 3 dB beamwidth of $35°$. The return signal is amplified and mixed with the transmit signal. This de-chirped signal is filtered and then sampled with a 16 bit A/D at 8.33 MHz. A custom FPGA board was designed to sample the signal and store the data on a pair of 32 GB Compact Flash disks. The data is collected continuously at a rate of 133 Mb/s and stored on-board. After hardware presumming, the effective PRF is 500 Hz.

Fig. 9 *Left*: Photograph of antennas mounted on a helicopter, and *right*: SAR system hardware
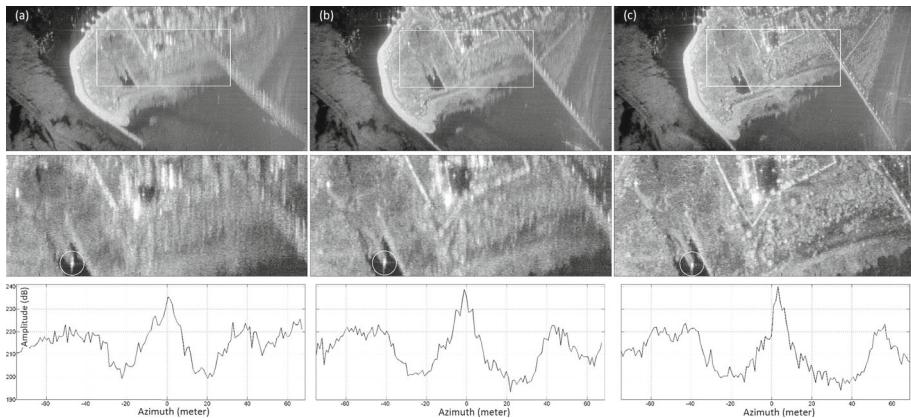

Fig. 10 A sample SAR image **a** without MC, **b** MC with navigation data, and **c** the proposed autofocus. *Middle row*: Magnified images highlighted by *white rectangles*. *Bottom row*: Azimuth profiles of selected point targets highlighted by *white circles*

It was not equipped with highly accurate inertial navigation units and the navigation depended merely on a GPS system. The GPS provided motion information at the frequency of 10 Hz, and its positioning accuracy of GPS was 5 m. Owing to the limitation and inaccuracy of the motion information, navigation-based MC was insufficient for the generation of the high quality imagery. Therefore, we needed a highly precise raw-data-based autofocus. The images generated by the GPS-based MC and our autofocus approach are shown in Fig. 10b, c, respectively. The vertical direction is azimuth, and the horizontal direction is range. Apparently, it can be noted that the image generated by the GPS-based MC is seriously blurred and distorted in geometry due to the lack and inaccuracy of motion measurements. While the image achieved by our autofocus approach is focused with a high quality. The area under observation is strongly diverse partly sea, coast, and town.

By compensating the spatially variant phases, the SAR imagery could be achieved with high precision. The local scene, highlighted in Fig. 10c by white rectangle, is amplified in Fig. 10 middle row. There are groups of corner reflectors array in the right corner of image. As clearly presented in the magnified image of Fig. 10c, the corner reflector arrays are focused
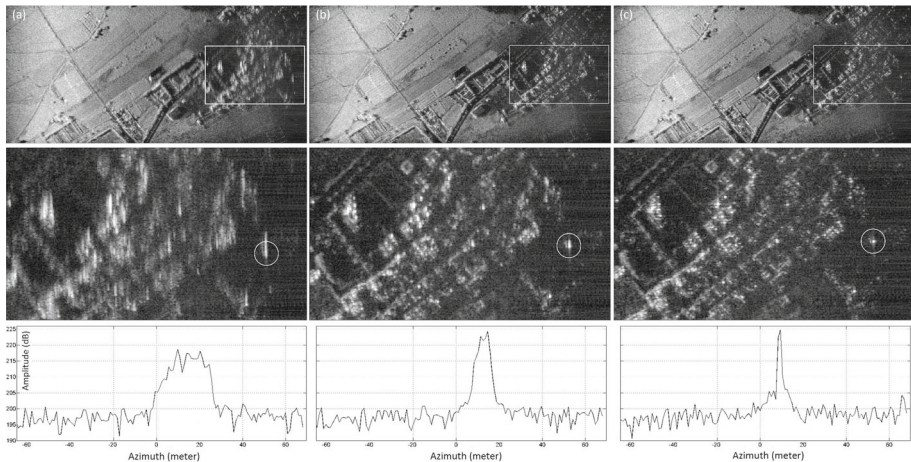
Fig. 11 A sample SAR image **a** without MC, **b** MC with navigation data, and **c** the proposed autofocus. *Middle row*: Magnified images highlighted by *white rectangles*. *Bottom row*: Azimuth profiles of selected point targets highlighted by *white circles*

in a good way. In addition, a point target has been selected to show the azimuth profile in different scenarios.

The presented method also works well in areas with several PPs. An example of a focused SAR image, created using the BP algorithm plus the proposed autofocus technique, is shown in Fig. 11c. From Fig. 11c, one can see the towns, freeway, villages, and wild scenes clearly distinguished and well-focused. For better demonstration, we have put the azimuth profiles of selected point targets highlighted by white circles in Figs. 10 and 11 in different scenarios on a same graph in Fig. 12. It can be seen from the results that the target impulse response in azimuth direction becomes narrower with higher peak level for our autofocus approach. The presented algorithm was also tested at a homogenous area with smaller PPs (see Fig. 13).

In the following, we have presented the experimental results of the microASAR imagery of CASIE-09 dataset (Edwards et al. 2008; Stringham and Long 2011). It provides a resolution of 1×1 m (range × azimuth). The microASAR is based on licensed BYU μSAR (Zaugg et al. 2006) technology. It is professionally built by ARTEMIS, Inc., making it a much more robust and flexible system (Edwards 2009). The MicroASAR is a complete, self-contained SAR system that has been designed specifically to be small and lightweight while still being robust and capable. These characteristics make it an ideal SAR system for use on UAS and other small aircraft. Rather than transmitting pulses, the MicroASAR is a continuous wave (CW) SAR system. A CW system is constantly transmitting and receiving and is thus capable of maintaining a high SNR while transmitting much less peak power than a comparable pulsed system. The microASAR transmits at 1 W and operates at altitudes 1,000–3,000 ft. It operates at C-band with a variable bandwidth up to 200 MHz. An analog de-chirp on receive reduces the sampling requirements to keep the data rate low. The system is pseudo-monostatic, i.e., it transmits and receives at the same time using two separate antennas that are placed closely together. This enables long transmit chips, which maximize the SNR while minimizing peak transmit power. The return signal is mixed down with a frequency-shifted copy of the transmit signal (this is known as analog dechirp), digitized, and processed with an all-digital IF stage. Raw data is stored into a compact flash (CF) disk along with GPS timing and position data. Using 32 GB CF disks, over 2 h of SAR data can be recorded.
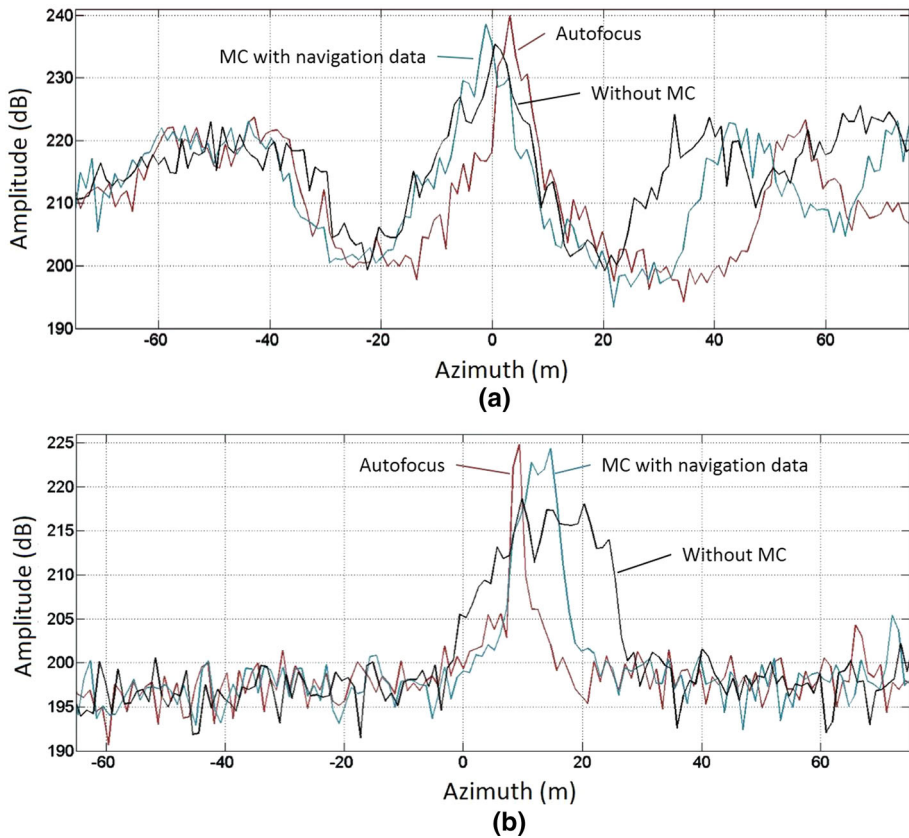
Fig. 12 Azimuth profiles of selected point targets in different scenarios highlighted by *white circles* in (**a**) Fig 10, and (**b**) Fig. 11
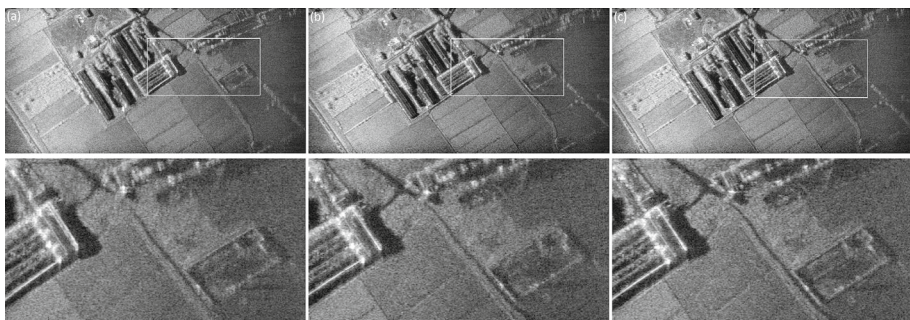

Fig. 13 A sample SAR image **a** without MC, **b** MC with navigation data, and **c** the proposed autofocus. *Bottom row*: Magnified images highlighted by *white rectangles*

In July 2009, a BYU/Artemis microASAR system was flown as part of the Characterization of Arctic Sea Ice Experiment 2009 (CASIE-09). An extensive data set of high resolution C-band SAR data was collected over sea ice by the microASAR from the NASA Sierra UAS 500 miles northwest of Svalbard Island in the Arctic Ocean. For the CASIE experiment,
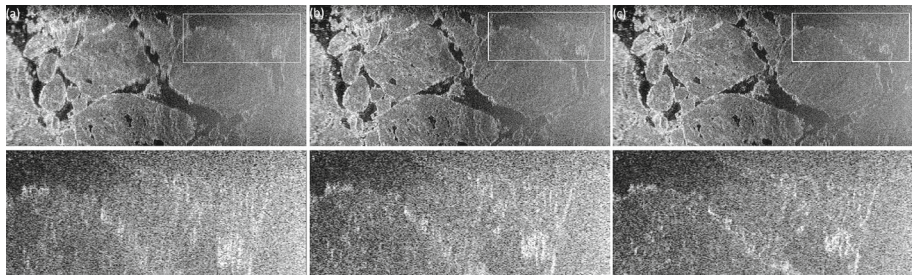
Fig. 14 A sample SAR image **a** without MC, **b** MC with navigation data, and **c** the proposed autofocus. *Bottom row*: Magnified images highlighted by *white rectangles*

the microASAR transmit bandwidth is set to 170 MHz, yielding a maximum ideal range resolution of approximately 90 cm, though the effective resolution is reduced in processing. The transmit center frequency is 5.42876 GHz. After hardware presumming, the effective PRF is 307.292 Hz. A short sample of the raw microASAR data is being made available as a public service, which is used here for second experiment.

The SAR image has been obtained by using the recorded motion parameters from the navigation system, as shown in Fig. 14b. In Fig. 14c, the image generated by applying the proposed autofocus approach, is presented. The horizontal direction is range, and the vertical direction is azimuth. In comparison, the magnified images of the scene highlighted by white rectangles are shown in Fig. 14 bottom row. Obviously, the image generated by the MC is blurred and distorted due to the inaccuracy of motion recording. However, the image generated by the proposed autofocus is well-focused. This experiment validates our method for another scenario of UAS SAR imagery, which is used for sea ice observation purpose.

6 Conclusions

This paper presents an autofocus method compatible with the SAR BP image formation algorithm. The proposed autofocus, which is a parametric-based method, utilizes genetic optimization algorithm with a new cost function to find an optimal flight trajectory. The cost function is obtained using PPs in different sub-apertures of SAR image. Thus, this autofocus method is well suited to BP image formation and its versatile imaging geometries. This autofocus method is advantageous because it requires no general assumptions of platform motion in order to operate. In addition, this new method can be used for both time and frequency domain algorithms. For frequency domain algorithm like RDA, the optimized flight trajectory can be used in the MC step.

The computational complexity of the proposed method is lower than the traditional parametric-based autofocus algorithm. This is because of two reasons: 1) it forms SAR image in limited range bins corresponding to PPs in each iteration of optimization algorithm instead of generating whole SAR image, and 2) it avoids RCMC step in RDA algorithm for image formation in the optimization loop because of modifying range-compressed data.

The proposed algorithm is especially important when a SAR is operated on a small aircraft or UAS, which are especially susceptible to the effects of atmospheric turbulence. The results on real LFM-CW SAR data show the validity of the proposed autofocus approach for BP algorithm.

References

Ash, J. N. (2012). An autofocus method for backprojection imagery in synthetic aperture radar. *IEEE Geoscience and Remote Sensing Letters*, *9*(1), 104–108.

Carrara, W. G., Goodman, R. S., & Majewski, R. M. (1995). *Spotlight synthetic aperture radar signal processing algorithms*. Boston, MA: Artech House.

Cumming, G., & Wong, F. H. (2005). *Digital processing of synthetic aperture radar data algorithms and implementation*. Norwood, MA: Artech House.

Cumming, G., Neo, Y. L., & Wong, F. (2003). Interpretations of the Omega-K algorithm and comparisons with other algorithms. In *Proceedings of the IEEE international geoscience and remote sensing symposium* (Vol. 3, pp. 1455–1458).

Edrich, M. (2004). Design overview and flight test results of the miniaturised SAR sensor MISAR. In *Proceedings of the first European radar conference* (pp. 205–208).

Edwards, M., Madsen, D., Stringham, C., Margulis, A., Wicks, B., & Long, D. (2008). MicroASAR: A small, robust LFM-CW SAR for operation on UAVs and small aircraft. In *Proceedings of the IEEE International Geoscience and Remote Sensing Symposium* (Vol. 5, pp. 514–517).

Edwards, M. C. (2009). Design of a continuous-wave synthetic aperture radar system with analog dechirp. Master's thesis, Brigham Young University.

Franceschetti, G., & Lanari, R. (1999). *Synthetic aperture radar processing*. Boca Raton, FL: CRC Press.

Frey, O., Magnard, C., Rüegg, M., & Meier, E. (2009). Focusing of airborne synthetic aperture radar data from highly nonlinear flight tracks. *IEEE Transactions on Geoscience and Remote Sensing*, *47*(6), 1844–1858.

Gilmore, C. G. (2004). A comparison of imaging methods using GPR for landmine detection and a preliminary investigation into the SEM for identification of buried objects. Master thesis, University of Manitoba Winnipeg, Manitoba, Canada.

Goldberg, E. (1989). *Genetic algorithms in search. Optimization & machine learning*. Reading: Addison-Wesley.

Hellsten, H., Dammert, P., & Ahlander, A. (2010). Autofocus in fast factorized backprojection for processing of SAR images when geometry parameters are unknown. In *IEEE radar conference* (pp. 603–608).

Horemuz, M., & Andersson, J. V. (2006). Polynomial interpolation of GPS satellite coordinates. *GPS Solutions*, *10*, 67–72.

Kennedy, J., & Eberhart, R. C. (1997). A discrete binary version of the particle swarm algorithm. In *Proceedings of the 1997 IEEE conference on systems, man, and cybernetics, Piscataway, NJ* (pp. 4104–4109).

Kirkpatrick, S., Gelatt, C. D., & Vecchi, M. P. (1983). Optimization by simulated annealing. *Science*, *220*, 671–680.

Krishnan, S. (2000). Modeling and simulation analysis of an FMCW radar for measuring snow thickness. Master thesis, University of Madras.

Liu, M., Li, Ch., & Shi, X. (2011). A back-projection fast autofocus algorithm based on minimum entropy for SAR imaging. In *3rd international Asia-Pacific conference on synthetic aperture radar (APSAR)* (pp. 1–4).

Meta, A., de-Wit, J., & Hoogeboom, P. (2004). Development of a high resolution airborne millimeter wave FM-CW SAR. In *Proceedings of the first European radar conference* (pp. 209–212).

Meta, A., Hakkaart, P., Zwan, F., Hoogeboom, P., & Ligthart, L. (2006). First demonstration of an X-band airborne FMCW SAR. In *Proceedings of the 6th European conference on synthetic aperture radar*.

Meta, A., Hoogeboom, P., & Ligthart, L. P. (2007). Signal processing for FMCW SAR. *IEEE Transactions on Geoscience and Remote Sensing*, *45*(11), 3519–3532.

Oliver, C., & Quegan, S. (1999). *Understanding synthetic aperture radar images*. Norwood, MA: Artech House.

Partida, J. T. G., Gonzalez, P. A., Garcia, M. B., & Naranjo, B. P. D. (2008). SAR system for UAV operation with motion error compensation beyond the resolution cell. *Sensors*, *8*(5), 3384–3405.

Rao, S. (1984). *Optimization: Theory and applications*. New York: Wiley.

Sandia. (2006). What is synthetic aperture radar. Internet Source, February. Sandia http://www.sandia.gov/RADAR/whatis.html

Schenewerk, M. (2003). A brief review of basic GPS orbit interpolation strategies. *GPS Solutions*, *6*, 265–267.

Stringham, C., & Long, D.G. (2011). Improved processing of the CASIE SAR data. In *IEEE International Geoscience and Remote Sensing Symposium*.

Wahl, D. E., Eichel, P. H., Ghiglia, D. C., & Jakowatz, C. V, Jr. (1994). Phase gradient autofocus—A robust tool for high resolution phase correction. *IEEE Transactions on Aerospace and Electronic Systems*, *30*(3), 827–835.

Wang, W., Peng, Q., & Cai, J. (2009). Waveform-diversity-based millimeter wave UAV SAR remote sensing. *IEEE Transactions on Geoscience and Remote Sensing*, *47*(3), 691–700.

Zaugg, E., Hudson, D., & Long, D. (2006). The BYU uSAR: A small, student-built SARfor UAV operation. In *Proceedings of the IEEE international geoscience and remote sensing symposium* (pp. 411–414).
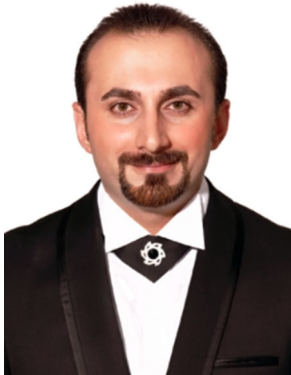
Jamal Saeedi was born in Amol, Iran, in 1984. He received the B.Sc. degree in Biomedical Engineering from Sahand University of Tabriz, Iran in 2007 and M.Sc. degree in Electronic Engineering from Amirkabir University of Tehran, Iran in 2010. He is currently a Ph.D. candidate in the Electrical Engineering Department of Amirkabir University of Technology, Tehran, Iran. He works in the field of signal and image processing, specializing particularly in image fusion, speech processing, biomedical signal compression, fuzzy image processing, radar signal processing, radar jamming and deception, and synthetic aperture radar imaging.

Karim Faez was born in Semnan, Iran. He received his B.S. degree in Electrical Engineering from Tehran Polytechnic University as the first rank in June 1973, and his M.S. and Ph.D. degrees in Computer Science from University of California at Los Angeles (UCLA) in 1977 and 1980, respectively. Prof. Faez was with Iran Telecommunication Research Center (1981–1983) before joining Amirkabir University of Technology (Tehran Polytechnic) in Iran, where he is now a professor of Electrical Engineering. He was the founder of the Computer Engineering Department of Amirkabir University in 1989 and he has served as the first chairman during April 1989–September 1992. Professor Faez was the chairman of planning committee for Computer Engineering and Computer Science of Ministry of Science, Research and Technology (during 1988–1996). His research interests are in Pattern Recognition, Image Processing, Neural Networks, Signal Processing, Farsi Handwritten Processing, Computer Networks, and Hardware Design. He is a member of IEEE, IEICE, and ACM.